

Association between tissue hypoxia, perfusion restrictions, and microvascular architecture alterations with lesion-induced impairment of neurovascular coupling

Andreas Stadlbauer^{1,2} , Thomas M Kinfe^{1,3} ,
Max Zimmermann^{1,4}, Ilker Eyüpoglu¹, Nadja Brandner¹,
Michael Buchfelder¹, Moritz Zaiss⁵, Arnd Dörfler⁵ and
Sebastian Brandner¹

Journal of Cerebral Blood Flow & Metabolism
2022, Vol. 42(3) 526–539
© The Author(s) 2020
Article reuse guidelines:
sagepub.com/journals-permissions
DOI: 10.1177/0271678X20947546
journals.sagepub.com/home/jcbfm



Abstract

Functional magnetic resonance imaging (fMRI) has been mainly utilized for the preoperative localization of eloquent cortical areas. However, lesion-induced impairment of neurovascular coupling (NVC) in the lesion border zone may lead to false-negative fMRI results. The purpose of this study was to determine physiological factors impacting the NVC. Twenty patients suffering from brain lesions were preoperatively examined using multimodal neuroimaging including fMRI, magnetoencephalography (MEG) during language or sensorimotor tasks (depending on lesion location), and a novel physiologic MRI approach for the combined quantification of oxygen metabolism, perfusion state, and microvascular architecture. Congruence of brain activity patterns between fMRI and MEG were found in 13 patients. In contrast, we observed missing fMRI activity in perilesional cortex that demonstrated MEG activity in seven patients, which was interpreted as lesion-induced impairment of NVC. In these brain regions with impaired NVC, physiologic MRI revealed significant brain tissue hypoxia, as well as significantly decreased macro- and microvascular perfusion and microvascular architecture. We demonstrated that perilesional hypoxia with reduced vascular perfusion and architecture is associated with lesion-induced impairment of NVC. Our physiologic MRI approach is a clinically applicable method for preoperative risk assessment for the presence of false-negative fMRI results and may prevent severe postoperative functional deficits.

Keywords

Blood-oxygen-level-dependent contrast, functional magnetic resonance imaging, hypoxia, magnetoencephalography, neurovascular coupling

Received 13 February 2020; Revised 1 July 2020; Accepted 15 July 2020

Introduction

Functional magnetic resonance imaging (fMRI) using the blood-oxygen-level-dependent (BOLD) contrast mechanism is one of the dominant in vivo imaging techniques to noninvasively visualize neural activity.^{1,2} This is mainly due to the fact that BOLD fMRI is characterized by easy implementation and widespread availability combined with relatively high sensitivity and spatial resolution. Cerebral blood flow (CBF) is locally controlled by the neurovascular unit in response to dynamic changes in tissue oxygen tension evoked by stimulus- or task-associated cortex activity: Increased

¹Department of Neurosurgery, Friedrich-Alexander University (FAU) of Erlangen-Nürnberg, Erlangen, Germany

²Institute of Medical Radiology, University Clinic of St. Pölten, St. Pölten, Austria

³Division of Functional Neurosurgery and Stereotaxy, Friedrich-Alexander University (FAU) of Erlangen-Nürnberg, Erlangen, Germany

⁴Department of Preclinical Imaging and Radiopharmacy, University of Tübingen, Tübingen, Germany

⁵Department of Neuroradiology, Friedrich-Alexander University of Erlangen-Nürnberg, Erlangen, Germany

Corresponding author:

Andreas Stadlbauer, Department of Neurosurgery, Friedrich-Alexander University of Erlangen-Nürnberg, Schwabachanlage 6, 91054 Erlangen, Germany.

Email: andi@nmr.at

extraction of oxygen from the local capillaries leads to a drop in oxygenated hemoglobin (oxyHb) and an increase in local carbon dioxide (CO₂) and deoxygenated hemoglobin (deoxyHb). The hemodynamic response of the neurovascular unit eventually overcompensates for this initial oxygen demand, resulting in a net decrease in local deoxyHb concentration and a net increase in local oxyHb.³ This large rebound in local blood and tissue oxygenation is detectable with BOLD fMRI because of the differences in magnetic susceptibility between oxyHb (diamagnetic) and deoxyHb (paramagnetic).^{4,5} Saying so, BOLD fMRI assesses neuronal activity via the hemodynamic response of the neurovascular unit, which is also known as neurovascular coupling (NVC). However, the BOLD effect may not be appropriately correlated with neuronal activity and local pathologic alterations in cerebral blood perfusion, tissue oxygen metabolism, and/or microvascular architecture, which may have a considerable influence on BOLD fMRI findings.

Neurosurgical procedures adjacent to functional important brain circuits are associated with a meaningful risk for the occurrence of postoperative neurological impairment and, therefore, still represent an unmet issue for preoperative decision-making. BOLD fMRI is the method of choice for the presurgical localization of eloquent cortex areas in the vicinity of brain lesions and is of high relevance for an effective surgical management.⁶ Of note, most brain lesions can affect BOLD fMRI due to lesion-induced impairment of NVC, and thus attenuation of the BOLD response.⁷ This can lead to false-negative results for localization of functional areas and, in further consequence, to a seriously deteriorated neurological postsurgical state.⁸

Magnetoencephalography (MEG) directly measures magnetic fields generated by the electrical currents produced by synchronous activity of thousands of neurons, well known as the local field potentials.⁹ Most importantly in our context, these electromagnetic recordings are unaffected by lesion-induced impairment of the NVC. While both methods have a spatial resolution in the mm range, MEG provides high-scale temporal resolution in the range of milliseconds (i.e. at the level of electrophysiological dynamics), contrary to fMRI with a time resolution in the range of seconds. However, due to its limited availability and time-consuming implementation of the presurgical tasks, MEG is not commonly applied in neurosurgical practice. Given these facts, only few studies^{10–12} combined BOLD fMRI with MEG experiments for the detection of an impaired NVC so far.

Alterations in local hemodynamics^{8,13,14} or oxygen availability¹⁵ have been previously described as the physiological correlate of impaired NVC. The interplay between blood perfusion (i.e. hemodynamics),

microvascular architecture, and oxygen metabolism (including tissue hypoxia) is of crucial importance for elucidating the physiological status of cortical regions adjacent to brain lesions. Most of the available techniques, however, are not well suited for *in vivo* characterization in humans due to their invasiveness (electrodes), limited availability and high costs (¹⁵O₂ positron emission tomography), or low spatial resolution (near-infrared spectroscopy). In our previously published study, we could demonstrate that a novel multiparametric MRI approach reliably allowed for the combined assessment of local perfusion, microvascular architecture, and oxygen metabolism in noninvasive manner.¹⁶ Hence, this method unifies microvascular architecture mapping (VAM)¹⁷ with multiparametric quantitative BOLD (qBOLD) MRI.¹⁸ VAM is based on the different sensitivity of gradient-echo (GE) and spin-echo (SE) MR imaging to magnetic susceptibility that provides additional characteristics relevant to the tissue microvascularity.^{19–21} Furthermore, a multiparametric qBOLD approach was proposed to gather quantitative information related to the oxygen metabolism and tissue oxygenation.¹⁸ In our previously performed studies, this approach was used to assess the tumor microenvironment of brain tumors and its changes during therapy and recurrence.^{22–26}

However, no previous study investigated alterations in both local hemodynamics and oxygen metabolism or included investigations of the microvascular architecture. In this study, we used a multimodal approach combining preoperative BOLD fMRI and MEG experiments for detection of lesion-induced impairment of NVC with physiological MRI measurements of perfusion, microvascular architecture, and oxygen metabolism in patients with brain lesions in order to investigate the physiological reasons of impaired NVC.

Materials and methods

Patients and histopathology

The study protocol was approved by the ethics committee of the University of Erlangen-Nürnberg and was in line with the Helsinki Declaration of Human Rights. Informed consent was obtained from all subjects. Twenty adult patients (13 male, 7 female; mean age ± standard deviation: 49.6 ± 16.2 years; age range: 24–76 years) with brain lesions were enrolled. The study cohort comprised 16 patients with histopathological confirmed glioma: 7 glioblastoma (GB, World Health Organization (WHO) grade IV), 3 anaplastic astrocytoma (AA, WHO grade III), 3 anaplastic oligodendroglioma (AOG, WHO grade III), 2 low-grade astrocytoma (WHO grade II), and 1 ganglioglioma

(WHO grade I), respectively. Furthermore, two patients suffered from an arteriovenous malformation (AVM), one patient suffered from a cavernoma (Cav), and one patient from a meningioma, respectively. Clinical details of the patients are summarized in Table 1.

Physiologic MRI data acquisition

Anatomic and physiologic MRI examinations were performed on a 3 tesla clinical scanner (Tim Trio, Siemens, Erlangen, Germany) equipped with a 32-channel head coil. The state-of-the-art MRI protocol included T_2 -weighted, diffusion-weighted (DWI), fluid-attenuated inversion-recovery, and pre- and post-contrast enhanced T_1 -weighted MRI, respectively. In addition, the following sequences were performed for physiologic MRI data acquisition: (i) a multiecho GE sequence for T_2^* -mapping (8 echoes; echo time (TE) = 5–40 ms; repetition time (TR) = 658 ms); (ii) a multiecho SE sequence for T_2 -mapping (8 echoes; TE = 12–96 ms; TR = 1610 ms); and (iii) a dynamic susceptibility contrast (DSC) bolus-tracking perfusion MRI sequence combined with a hybrid single-shot gradient-echo spin-echo (GESE) echo planar imaging

(EPI) readout (TR = 1380 ms; TE[GE] = 16 ms; TE [SE] = 89 ms) were performed.¹⁹ Geometric parameters were chosen identically for the three experimental sequences: axial slice orientation; field-of-view (FoV) = $230 \times 230 \text{ mm}^2$; in-plane resolution = $1.8 \times 1.8 \text{ mm}^2$; slice thickness = 4 mm; 8 slices. DSC GESE perfusion examinations were performed with 80 dynamic measurements during administration of a double dose (0.2 mmol/kg bodyweight) of gadoterate meglumine (Dotarem, Guerbet, France) at a rate of 4 ml/s followed by a 20-ml bolus of saline using an MR-compatible injector (Spectris, Medrad Bayer, Leverkusen, Germany). This resulted in 80 dynamic volumes of both GE-EPI and SE-EPI for tracking the first-pass peak contrast media bolus dynamics. The acquisition time (TA) for the three experimental sequences was less than 5 min: TA for T_2^* -mapping = 50 s; TA for T_2 -mapping = 2.0 min; and TA for DSC GESE perfusion = 1.8 min. The total MRI TA was about 30 min.

Physiologic MRI data processing

Processing of physiologic MRI data and calculation of MRI biomarker maps for oxygen metabolism,

Table 1. Clinical details of the patients.

ID	Age (y)	Sex	Histo	Location of the lesion	LVol (cm ³)	Neurol. deficits		ShDi (mm)	Impaired NVC	funct. task	r thresh.
						preop	postop				
1	55	m	Men	l temporal	48.9	no	no	0	no	lang	0.3
2	76	m	GB	r frontal	77.9	no	no	2	yes	sm	0.13
3	67	m	AOG	l frontal	102	no	no	22	yes	lang	0.12
4	54	m	GB	r trigonal	58.1	yes	no	9	yes	sm	0.21
5	41	m	AA	l parietal	71.7	no	no	4	no	sm	0.3
6	59	m	GB	r temporal	232	yes	no	13	yes	sm	0.17
7	71	m	GB	l temporal	24.6	no	no	8	no	lang	0.3
8	43	m	AOG	r central	40.2	yes	no	0	no	sm	0.3
9	31	m	LGA	l frontal	29.9	no	no	4	no	lang	0.3
10	36	f	AVM	r temporal	0.3	no	no	2	no	sm	0.3
11	73	m	Cav	l temporal	5.9	no	no	0	yes	lang	0.16
12	44	m	AVM	l postcentral	7.9	no	yes	0	no	sm	0.3
13	41	f	AOG	l frontal	67.0	yes	yes	5	no	sm	0.3
14	51	f	GB	r frontal	15.7	yes	no	2	yes	sm	0.18
15	27	m	AA	l fronto-insular	35.8	no	no	0	no	lang	0.3
16	58	f	GB	l temporal	36.7	no	yes*	9	no	lang	0.3
17	45	m	AA	l fronto-temp.	58.6	no	no	8	yes	lang	0.26
18	27	f	LGA	l frontal	3.0	no	yes*	0	no	lang	0.3
19	24	f	GG	l temporal	2.7	no	yes*	5	no	lang	0.3
20	68	f	GB	l frontal	53.2	yes	yes	0	no	lang	0.3

Histo: histology of the lesion; LVol: lesion volume; Neurol. deficits preop/postop: preoperative/postoperative neurologic deficits; ShDi: shortest distance between cortical area with important brain function and lesion border; NVC: neurovascular coupling; funct. task: functional task; lang: language task; sm: sensorimotor task; r thresh.: correlation threshold used for BOLD fMRI data evaluation. Note: numbers lesser than 0.3 are the reduced threshold values at that an fMRI activity was visible. Men: meningioma; GB: glioblastoma WHO grade IV; AOG: anaplastic oligodendroglioma WHO grade III; AA: anaplastic astrocytoma WHO grade III; GG: ganglioglioma WHO grade I; LGA: low-grade astrocytoma WHO grade II; AVM: arteriovenous malformation; Cav: cavernoma.

perfusion, and microvascular architecture were performed with custom-made MATLAB (MathWorks, Natick, MA, USA) software. Details about the whole data processing pipeline from MRI data acquisition over preprocessing to biomarker calculation were described previously.^{16,17,25} Briefly, qBOLD data processing included three steps: (i) corrections for background fields of the T2*-mapping data¹⁶ and for stimulated echoes of the R2-mapping data;²⁷ (ii) calculation of R2*- and R2 maps from the multiecho MR relaxometry data; and (iii) calculation of cerebral blood volume (CBV) and CBF maps from the GE-EPI DSC perfusion MRI data via automatic identification of arterial input functions (AIFs)²⁸ and correction for remaining contrast agent extravasation.²⁹ These data were used for the calculation of MRI biomarker maps of oxygen metabolism, including oxygen extraction fraction (OEF), cerebral metabolic rate of oxygen (CMRO₂), and the mitochondrial oxygen tension (mitoPO₂) using the following equations:^{18,30}

$$\text{OEF} = \frac{R_2^* - R_2}{4/3 \cdot \pi \cdot \gamma \cdot \Delta\chi \cdot \text{Hct} \cdot B_0 \cdot \text{CBV}}$$

with $R_2^* = 1/T_2^*$; $R_2 = 1/T_2$; $\gamma = 2.67502 \cdot 10^8$ rad/s/T is the nuclear gyromagnetic ratio; $\Delta\chi = 0.264 \cdot 10^{-6}$ is the difference between the magnetic susceptibilities of fully oxygenated and fully deoxygenated hemoglobin; $\text{Hct} = 0.42\text{--}0.85$ is the microvascular hematocrit fraction, whereby the factor 0.85 stands for a correction factor of systemic Hct for small vessels

$$\text{CMRO}_2 = \text{OEF} \cdot \text{CBF} \cdot C_a$$

where $C_a = 8.68$ mmol/ml is the arterial blood oxygen content,³¹ and

$$\text{mitoPO}_2 = P_{50} \left(\frac{2}{\text{OEF}} - 1 \right)^{1/h} - \frac{\text{CMRO}_2}{L}$$

where P_{50} is the hemoglobin half-saturation tension of oxygen (27 mmHg) and h is the Hill coefficient of oxygen binding to hemoglobin (2.7), and L (4.4 mmol/hg/min) is the tissue oxygen conductivity as defined by Vafaee and Gjedde.³²

In a next step, the calculation of microvascular CBV (μCBV) and microvascular CBF (μCBF) maps from the SE-EPI DSC perfusion MRI data via a separate automatic identification of AIFs was performed.²⁸

The data processing for the microvascular architecture was performed according to the following steps: (i) correction for remaining contrast agent extravasation;²⁹ (ii) fitting of the first bolus curves for each

voxel of the GE- and SE-DSC perfusion data with gamma-variate function;³³ and (iii) calculation of the $\Delta R_{2,\text{GE}}$ versus $(\Delta R_{2,\text{SE}})^{3/2}$ diagram¹⁹—the so-called vascular hysteresis loop (VHL). These data were used for calculation of MRI biomarker maps of the microvessel density (MVD) and vessel size index (VSI, i.e. the microvessel radius)³⁴ using the following equations:

$$\text{MVD} = \frac{Q_{\max}}{b} \cdot \left(\frac{\text{CBV}^2}{4\pi^2 \cdot \text{ADC} \cdot R^4} \right)^{1/3}, \text{ and}$$

$$\text{VSI} = \left(\frac{\text{CBV} \cdot \text{ADC} \cdot b^3}{2\pi \cdot Q_{\max}^3} \right)^{1/2}$$

with $Q_{\max} = \max[\Delta R_{2,\text{GE}}] / \max[(\Delta R_{2,\text{GE}})^{3/2}]$ obtained from the VHL; $-R \approx 3.0 \mu\text{m}$ is the mean vessel lumen radius; ADC is the apparent diffusion constant calculated from the DWI data; and b is a numerical constant ($b = 1.6781$).³⁴

Preoperative BOLD fMRI

BOLD fMRI data acquisition was performed on a 1.5 tesla whole-body MR scanner (Magnetom Sonata, Siemens, Erlangen, Germany), which is installed in an operating theater, using a conventional 2D EPI sequence with the following parameters: FoV = $192 \times 192 \text{ mm}^2$; acquisition matrix = 64×64 ; slice thickness = 3 mm; 16 slices, TE = 60 ms, TR = 2470 ms, flip angle = 90° . A block paradigm with 180 measurements in 6 blocks (3 resting state and 3 active intervals) with 30 volumes per block was used. The task that was performed by the patients depended on the lesion location, i.e. patients with lesions located in vicinity to the sensory-motor cortex performed a sensory-motor task, whereas patients with lesions in the vicinity of the cortical language areas performed a language task. The total examination time (including instruction and preparation of the patients) for the BOLD fMRI experiments was 1.5 to 2 h.

For localization of cortical motor areas, the patients were instructed to repeatedly flex and extend all digits (exercise 1) or foot and toes (exercise 2) of a designated side and to refrain from any other motor actions. Start and stop commands for the movements were given acoustically, and the patients' movements were monitored from the control room. In somatosensory measurements, the patients were asked to avoid any motor activity, and the stimulation of the index finger was started and stopped automatically according to the intervals. The sensory-motor task was described in more detail previously.³⁵

For localization of cortical language areas, the following two tasks were used: (i) Conjugation of a given verb in first person, past tense: 150 short verbs,

typically with one syllable, were used. Of this, 80% were irregular verbs, 20% were regular verbs. (ii) Building a simple sentence with a given noun: 150 short nouns, typically 4 to 5 letters long, were used. The language task was described in more detail previously.¹⁰

BOLD fMRI data processing was performed in three steps using a dedicated software package (BrainVoyager, Brain Innovation, Maastricht, the Netherlands): (i) Motion correction was performed using an image-based prospective acquisition correction applying interpolation in the k-space.³⁶ (ii) For determination of activated areas during each task, a gamma-variate function was convolved with the task reference function (time course of square waveform) and cross-correlated with the BOLD signal on a voxel-wise basis. Cortical activation was determined using a threshold of 0.30 corresponding to a Bonferroni corrected $p < 0.01$ (significance level of $p < 0.000045$).³⁷ Clusters of at least four contiguous voxels were assembled in order to eliminate isolated voxels and fused automatically to an anatomical data set (3-D T1w MRI).^{10,35} (iii) For detection of lesion-induced impairment of NVC in cortical areas with missing BOLD response which, however, were expected from MEG results (see below), these areas were analyzed by lowering the threshold from 0.3 progressively in 0.01 steps to 0.05 or until occurrence of a BOLD activation.

Additionally, in patients with existing BOLD response, the threshold was progressively increased from 0.1 to 0.7 in steps of 0.05 until disappearance of BOLD activations in the vicinity to the lesions.

Preoperative MEG

MEG experiments were performed prior to the MRI examinations; details were described previously.^{10,35} Briefly, cortical motor-evoked fields, somatosensory-evoked fields, or language-evoked fields were continually recorded using a 248-magnetometer whole-head MEG system (MAGNES 3600 WH, 4-D Neuroimaging, San Diego, CA, USA) installed in a magnetically shielded room (Vacuumschmelze, Hanau, Germany). MEG signals were acquired at a 678-Hz sampling rate using an online high-pass filter of 0.1 Hz, low-pass filter of 200 Hz, and noise cancellation. For co-registration of MEG data and anatomical MRI data, we used five small coils placed on the surface of the patients' head at defined positions, and digitization of the patients' head surface was performed using a 3-D tracking system (Polhemus, Colchester, VT, USA). The total examination time (including instruction and preparation of the patients) for the MEG experiments was about 2 h.

Motor and somatosensory MEG recordings were performed in the same session following the comprehensive sensorimotor protocol where external mechanic (sensory) stimulation serves as a cue for patients' movements as described previously.³⁸ Visual language stimulation was achieved using dedicated software (E-Prime, Psychology Software Tools, Sharpsburg, PA, USA). Language tasks were similar to those used in BOLD fMRI experiments: (i) conjugation of verbs and (ii) building of short sentences. The interstimulus intervals were 3000 ms. Patients were instructed to avoid any other motor actions like blinking, swallowing, or moving other parts of the body as effectively as possible. Patients were supervised using a camera installed in the shielded room.

Typically, 300 trials were recorded during each MEG experiment. Trials exhibiting artefacts originating from the patient or external noise were excluded by visual inspection from an experienced MEG investigator. All remaining trials with sufficient data quality (typically around 280) were averaged using a trigger signal for start of stimulation and filtered by band pass (0.3–95 Hz) and notch filter (50 Hz). The noise covariance data were calculated from baseline data in the 500 ms pretrigger interval. Individual brain MRI data (3-D T1w MRI) were used to create individual brain anatomy data set BrainSuite (version 15c)³⁹ in order to consider for lesion-induced changes in brain anatomy. Localization of MEG-based cortical activation was performed with dynamical Statistical Parametric Mapping (dSPM)⁴⁰ as part of the brainstorm software package (version 3.4).⁴¹ dSPM is based on minimal modeling to estimate distributed sources and are applicable on complex data sets or at high noise levels^{42,43} and uses deep weighting and noise normalization for compensation. Deep weighting was performed by normalizing all sources in the model using a measure of the overall amplitude. A minimization of the localization errors was achieved by normalization of rows of the lead field matrix.⁴⁰ Details for MEG data analysis were described previously.^{10,35}

Multimodal data and statistical analysis

Both fMRI- and MEG-based cortical localizations were displayed on an anatomical 3-D T1w MRI data set. The following cortical areas in the motor network were evaluated: M1, premotor area, and supplementary motor area. The evaluated cortical areas in the cortical somatosensory network were the primary and secondary somatosensory cortex. Cortical language areas included in total 13 subareas of Broca's area, Wernicke's area, the angular gyrus, and the supramarginal gyrus, respectively. Details about the language subareas were published previously.¹⁰ Areas of

motor, sensory, and language function were classified into three subgroups via comparison of the fMRI- and MEG-based cortical activity patterns: (i) cortical activity in both BOLD fMRI and MEG data on the ipsilateral side of the brain lesion; (ii) cortical activity in both BOLD fMRI and MEG data on the contralateral side of the brain lesion; and (iii) cortical activity in MEG data but not in BOLD fMRI data using the conventional threshold for correlation on the ipsilateral side of the brain lesion. The latter cortical areas were interpreted as impaired NVC in functional important brain areas.

Regions of interest (ROIs) were manually defined for the first and second subgroup of cortical localizations (BOLD and MEG ipsilateral, BOLD and MEG contralateral) on axial slices of the BOLD fMRI results bordering the whole cortical activation (see black contour line in Figure 1). For the third subgroup, the same procedure was performed on the MEG results (see black contour lines in Figure 2). The ROIs were subsequently transferred to the co-registered imaging biomarker maps for oxygen metabolism (OEF, CMRO₂, and mitoPO₂), perfusion (CBV, CBF, μ CBV, and μ CBF), and microvascular architecture (MVD and

VSI), respectively. Mean values of all imaging biomarkers as well as of the z score and the t score for the BOLD fMRI data were calculated for the ROIs and statistically analyzed using dedicated software (SPSS, IBM, Chicago, IL, USA). Differences in MRI biomarkers between subgroups of cortical areas were determined using the analysis of variance method. Dunnett's T3 test was used as post hoc procedure to be consistent with the assumption that homogeneity of variance was not met and for correction for multiple comparisons. Homogeneity of variance was tested using the Levene's test. Intraindividual differences in MRI biomarker values between ipsi- and contralateral cortical areas were compared using a Wilcoxon signed-rank test. Significance of differences in lesion volume and shortest distance of cortical function to lesion border between patient subgroups with or without impaired NVC was calculated using a Mann-Whitney U test. The Pearson's correlation coefficient (R) was calculated as a measure of the strength of the linear relationship between imaging biomarkers and z scores and the t scores, respectively. p values less than 0.05 were considered to indicate significance.

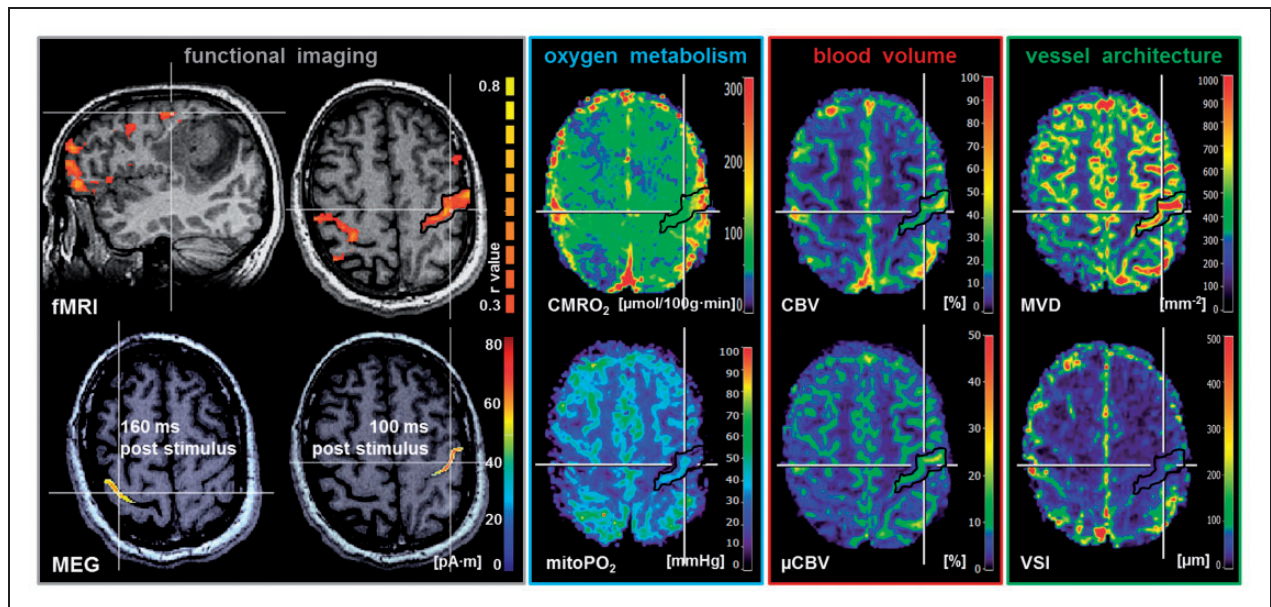


Figure 1. Multimodal imaging in a 41-year-old patient suffering from an anaplastic astrocytoma (ID 5 in Table 1) with intact NVC in the cortical areas for sensorimotor function. From left to right: BOLD fMRI-based cortical localizations superimposed onto T1w MRI data (in sagittal and axial orientation) showed good spatial congruence with the MEG-based findings measured 160 ms and 100 ms poststimulus, respectively. MR imaging biomarker maps for oxygen metabolism (CMRO₂ and mitoPO₂), cerebral blood volume (CBV and μ CBV), and microvascular architecture (MVD and VSI) revealed no alterations or restrictions and no significant differences between ipsi- and contralateral side to the lesion. Note: White lines indicate the slice intersections; black contour lines are the ROIs for data analysis; color coding bars are positioned on right-hand side of corresponding image. For the fMRI images, the color coding bar represents the correlation coefficient (r value).

fMRI: functional magnetic resonance imaging; MEG: magnetoencephalography; CMRO₂: cerebral metabolic rate of oxygen; mitoPO₂: mitochondrial oxygen tension; CBV: cerebral blood volume; μ CBV: microvascular cerebral blood volume; MVD: microvessel density; VSI: vessel size index.

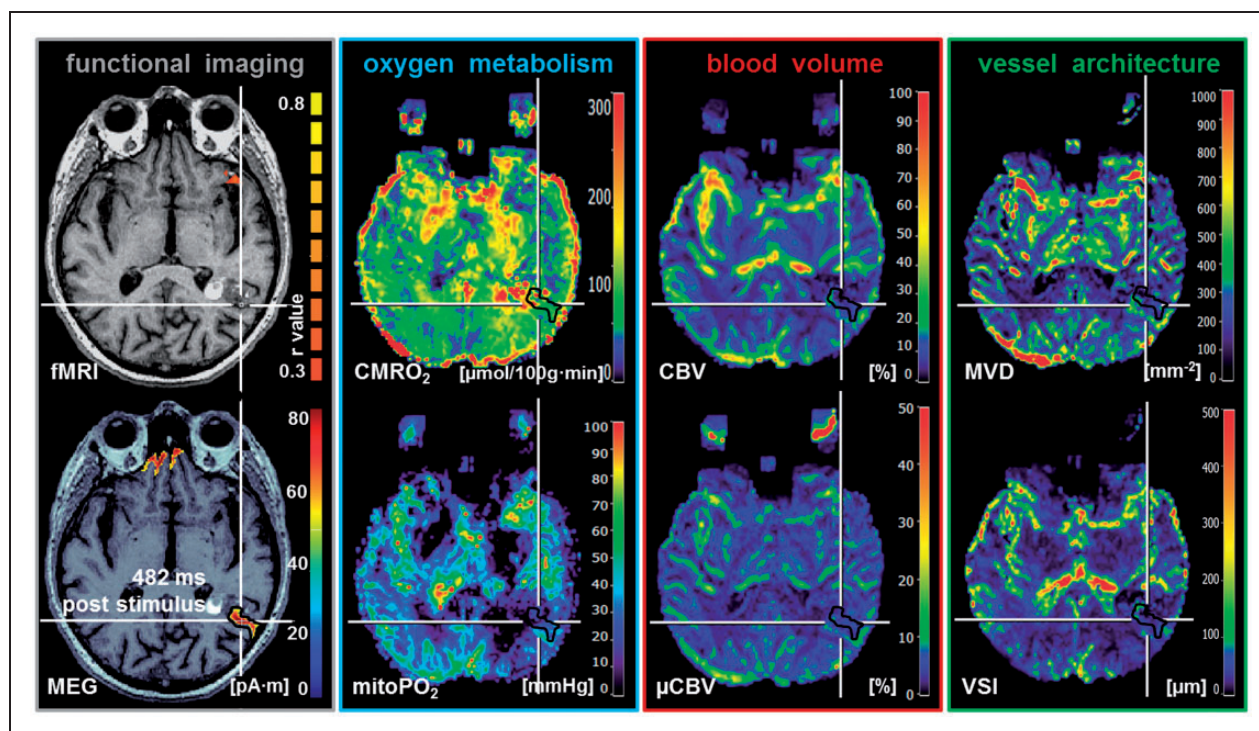


Figure 2. Multimodal imaging in a 73-year-old patient suffering from a Cav (ID 11 in Table 1) with impaired NVC in a cortical area for language function (posterior superior temporal sulcus (STS) extending into Brodmann's area 39). From left to right: BOLD fMRI-based cortical localizations superimposed onto axial T1w MRI data showed missing BOLD response when compared with MEG-based cortical localizations of language functions (482 ms poststimulus). MR imaging biomarker maps revealed alterations in oxygen metabolism (high CMRO₂ and low mitoPO₂) due to restrictions in cerebral blood volume (decreased CBV and μ CBV) and microvascular architecture (decreased MVD and VSI) compared to the contralateral side to the lesion. Note: White lines indicate the slice intersections; black contour lines are the ROIs for data analysis; color coding bars are positioned on right-hand side of corresponding image. For the fMRI image, the color coding bar represents the correlation coefficient (*r* value). fMRI: functional magnetic resonance imaging; MEG: magnetoencephalography; CMRO₂: cerebral metabolic rate of oxygen; mitoPO₂: mitochondrial oxygen tension; CBV: cerebral blood volume; μ CBV: microvascular cerebral blood volume; MVD: microvessel density; VSI: vessel size index.

Results

Differences in patient and lesion characteristics

Physiological MRI examinations as well as preoperative functional imaging with BOLD fMRI and MEG were successfully performed in all 20 patients. In accordance with the location of the brain lesion, 11 patients obtained multimodal functional imaging in combination with language tasks and 9 patients in combination with sensorimotor tasks, respectively. From the 20 patients, 13 patients showed good congruence between BOLD fMRI and MEG (Figure 1); however, 7 patients (35%) showed indications for impaired NVC (Figure 2), i.e. cortical activity in MEG data but not in BOLD fMRI data using the common threshold for correlation (> 0.3). In all seven patients, however, lowering of the threshold was associated with the appearance of BOLD activation, indicating a reduced BOLD

effect due to an impairment of the NVC. The lowered threshold values are summarized in Table 1.

From these seven patients with impaired NVC, three patients performed the language tasks and four patients the sensorimotor tasks, with four patients suffering from a GB (WHO grade IV) and one patient each from an AOG (WHO grade III), an AA (WHO grade III), and a Cav, respectively. Patients with low-grade glioma or AVMs showed no impaired NVC (Table 1).

Although we observed a difference in lesion volume between the subgroups of patients with intact NVC ($32.5 \pm 24.1 \text{ cm}^3$; $0.3\text{--}71.7 \text{ cm}^3$) and with impaired NVC ($78.5 \pm 75.4 \text{ cm}^3$; $5.9\text{--}231.9 \text{ cm}^3$), this was statistically not significant ($p = 0.081$). The shortest distance of cortical function to the brain lesion border was also not significant different ($p = 0.115$) between these subgroups: intact NVC: $2.8 \pm 3.2 \text{ mm}$, 0 to 9 mm; impaired NVC: $8.0 \pm 7.7 \text{ mm}$, 0 to 22 mm (Table 1).

Differences in physiologic MRI biomarkers

In the 13 patients with intact NVC, i.e. with reliable accordance between all fMRI- and MEG-based cortical localizations, we found no significant differences in physiologic MRI biomarkers comparing ipsi- and contralateral functional brain areas ($p=0.331-1.0$). An illustrative case for this patient subgroup is presented in Figure 1. However, in the seven patients with impaired NVC (i.e. missing BOLD response) in one functional brain region, all physiologic MRI biomarkers were significantly different ($p=0.017-0.028$) in these functional brain areas compared to the values of the functional brain regions contralateral to the side of the lesion. Furthermore, the physiologic MRI biomarkers in the functional brain areas with

impaired NVC were significantly different ($p=0.018-0.028$) compared to those in the functional brain areas on the ipsilateral side with intact NVC, except for $CMRO_2$ ($p=0.108$). Figure 2 illustrates an example out of this particular subgroup of patients. In general, OEF and $CMRO_2$ were increased, while all other biomarkers were decreased in functional brain areas with impaired NVC (Figure 3). In summary, functional brain areas with lesion-induced impairment of NVC showed increased oxygen metabolism but decreased blood perfusion as well as alterations in microvascular architecture, which resulted in a distinctly reduced tissue oxygen tension, i.e. hypoxia. No significant differences ($p=0.552-1.0$) were found between the subgroups of patients for the physiologic imaging biomarkers in the functional brain areas with intact

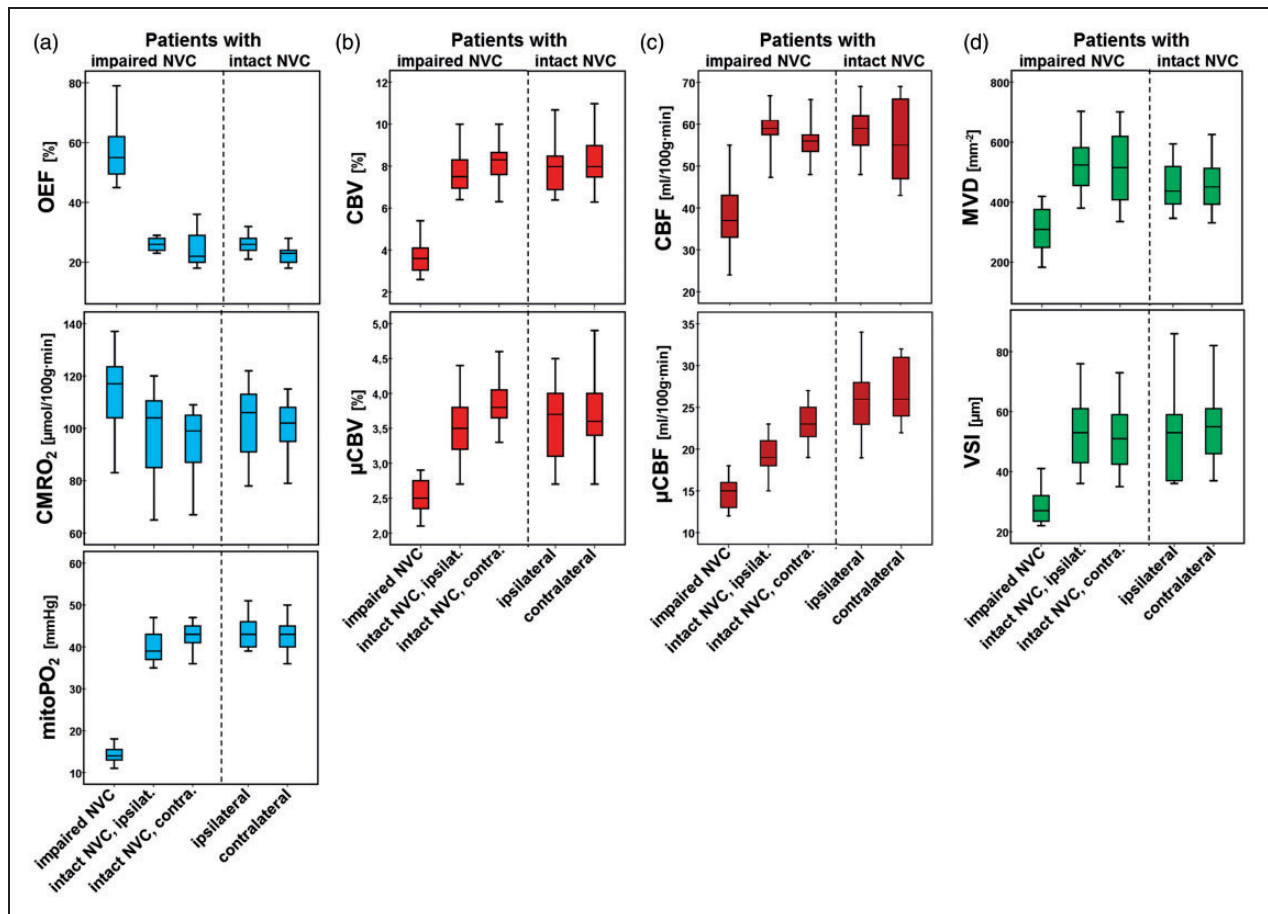


Figure 3. Box-whisker plots demonstrating the minimum, the maximum, the sample median, and the first and third quartiles of the MR imaging biomarker values for (a) oxygen metabolism (OEF, $CMRO_2$, and $mitoPO_2$), (b) cerebral blood volume (CBV and μCBV), (c) cerebral blood flow (CBF and μCBF), and (d) microvascular architecture (MVD and VSI), respectively. The values for the patients with an impaired NVC in a cortical region with important brain function are presented on the left-hand side of the individual panels. The values for the patients with intact NVC are presented on right-hand side separated by a dashed line from the former. NVC: neurovascular coupling; OEF: oxygen extraction fraction; $CMRO_2$: cerebral metabolic rate of oxygen; $mitoPO_2$: mitochondrial oxygen tension; CBV: cerebral blood volume; μCBV : microvascular cerebral blood volume; CBF: cerebral blood flow; μCBF : microvascular cerebral blood flow; MVD: microvessel density; VSI: vessel size index.

NVC (ipsi- and contralateral). Table 2 displays the physiologic MRI biomarker values for the two subgroups of patients.

Investigation of attenuated BOLD responses

For the patients with impaired NVC, both the z score and the t score from BOLD fMRI data were calculated for the cortical areas with an attenuated BOLD response. For the patients with intact NVC, z score and the t score values were calculated for the cortical areas in closest vicinity to the lesion. Both z score and the t score values were correlated with the corresponding physiologic MRI biomarker values in the same ROI. For all 20 patients together, the z score showed a significant correlation ($R = -0.770-0.802$; $p < 0.001$ to 0.03) with all physiologic MRI biomarkers, except for $CMRO_2$, which revealed no significant correlation ($R = -0.136$; $p = 0.569$). The t score, however, additionally showed no significant correlation with CBF ($R = 0.421$; $p = 0.065$), MVD ($R = 0.335$; $p = 0.149$), and VSI ($R = 0.401$; $p = 0.080$), respectively. For the patient subgroups with impaired and intact NVC, respectively, we found no significant correlations between BOLD fMRI metrics (z and t score) and the physiologic MRI biomarker values. The correlation coefficients between the BOLD fMRI metrics and the

physiologic MRI biomarkers are summarized in Table 3.

Figure 4 depicts the relationship between the number of patients with signs of impaired NVC and the r value threshold used for BOLD fMRI data processing. A value of 0.3 is commonly used as threshold for correlation. As expected, an increase in the r value threshold was associated with an increase in the assigned number of patients with signs of impaired NVC. Interestingly, an increase of the threshold from 0.3 to 0.35 showed no increase in the number of patients with signs of impaired NVC. This might be interpreted that a threshold of 0.3 is a good compromise for a common threshold for preclinical functional mapping in clinical routine

Discussion

In this study, we attempt to investigate the physiological basis for an impaired NVC using a multimodal neuroimaging approach that combined preoperative BOLD fMRI and MEG experiments for detection of lesion-induced attenuation of the BOLD effect with physiological MRI measurements of hemodynamics, microvascular architecture, and oxygen metabolism in patients with brain lesions. In one third of patients, we observed impairment of NVC in perilesional brain

Table 2. MR imaging biomarker values for oxygen metabolism, perfusion, and microvascular architecture in the patient subgroups with impaired and intact NVC.

	Patients with impaired NVC			Patients with intact NVC	
	Impaired NVC	Intact NVC, ipsilateral	Intact NVC, contralateral	Ipsilateral	Contralateral
OEF (%)	57 ± 12 (45–79)	26 ± 2 (23–29)	25 ± 7 (18–36)	26 ± 3 (21–32)	23 ± 3 (18–28)
CMRO ₂ (μmol/100g·min)	113 ± 18 (83–137)	97 ± 21 (65–120)	94 ± 16 (67–109)	103 ± 14 (78–122)	100 ± 11 (79–115)
mitoPO ₂ (mmHg)	14 ± 2 (11–18)	40 ± 5 (35–47)	43 ± 4 (36–47)	44 ± 4 (39–51)	43 ± 4 (36–50)
CBV (%)	3.7 ± 1.0 (2.6–5.4)	7.8 ± 1.2 (6.4–10.0)	8.2 ± 1.2 (6.3–10.0)	7.9 ± 1.3 (6.4–10.7)	8.4 ± 1.4 (6.3–11.0)
μCBV (%)	2.5 ± 0.3 (2.1–2.9)	3.5 ± 0.6 (2.7–4.4)	3.9 ± 0.4 (3.3–4.6)	3.6 ± 0.5 (2.7–4.5)	3.7 ± 0.6 (2.7–5.0)
CBF (ml/100g·min)	38 ± 11 (24–55)	59 ± 6 (47–67)	56 ± 6 (48–66)	59 ± 7 (48–69)	55 ± 10 (43–69)
μCBF (ml/100g·min)	15 ± 2 (12–18)	22 ± 3 (18–28)	23 ± 3 (19–27)	26 ± 5 (19–34)	27 ± 4 (22–32)
MVD (mm ⁻²)	309 ± 91 (183–419)	526 ± 111 (380–703)	515 ± 147 (335–701)	453 ± 76 (347–596)	466 ± 94 (332–627)
VSI (μm)	29 ± 7 (22–41)	53 ± 14 (36–76)	52 ± 14 (35–73)	53 ± 17 (36–86)	55 ± 12 (37–82)

NVC: neurovascular coupling; OEF: oxygen extraction fraction; CMRO₂: cerebral metabolic rate of oxygen; mitoPO₂: mitochondrial oxygen tension; CBV: cerebral blood volume; μCBV: cerebral blood volume in microvasculature; CBF: cerebral blood flow; μCBF: cerebral blood flow in microvasculature; MVD: microvessel density; VSI: vessel size index.

Table 3. Correlation coefficients between MR imaging biomarker values and BOLD fMRI metrics for all patients as well as for the patient subgroups with impaired and intact NVC.

	All patients		Patients with impaired NVC		Patients with intact NVC	
	z score	t score	z score	t score	z score	t score
OEF (%)	-0.770 (<i>p</i> < 0.001)	-0.632 (<i>p</i> = 0.003)	-0.581 (<i>p</i> = 0.171)	-0.620 (<i>p</i> = 0.138)	0.354 (<i>p</i> = 0.235)	0.131 (<i>p</i> = 0.670)
CMRO ₂ (μmol/100g·min)	-0.136 (<i>p</i> = 0.569)	0.068 (<i>p</i> = 0.777)	0.094 (<i>p</i> = 0.840)	0.166 (<i>p</i> = 0.722)	0.280 (<i>p</i> = 0.354)	0.474 (<i>p</i> = 0.102)
mitoPO ₂ (mmHg)	0.802 (<i>p</i> < 0.001)	0.619 (<i>p</i> = 0.004)	-0.144 (<i>p</i> = 0.759)	-0.185 (<i>p</i> = 0.692)	0.038 (<i>p</i> = 0.902)	-0.029 (<i>p</i> = 0.924)
CBV (%)	0.683 (<i>p</i> = 0.001)	0.538 (<i>p</i> = 0.014)	-0.115 (<i>p</i> = 0.806)	0.036 (<i>p</i> = 0.938)	-0.144 (<i>p</i> = 0.638)	-0.094 (<i>p</i> = 0.761)
μCBV (%)	0.564 (<i>p</i> = 0.010)	0.616 (<i>p</i> = 0.004)	-0.076 (<i>p</i> = 0.871)	-0.125 (<i>p</i> = 0.789)	-0.126 (<i>p</i> = 0.682)	0.318 (<i>p</i> = 0.290)
CBF (ml/100g·min)	0.543 (<i>p</i> = 0.013)	0.421 (<i>p</i> = 0.065)	-0.199 (<i>p</i> = 0.669)	-0.044 (<i>p</i> = 0.925)	-0.397 (<i>p</i> = 0.179)	-0.274 (<i>p</i> = 0.365)
μCBF (ml/100g·min)	0.696 (<i>p</i> = 0.001)	0.578 (<i>p</i> = 0.008)	-0.145 (<i>p</i> = 0.757)	0.162 (<i>p</i> = 0.729)	0.130 (<i>p</i> = 0.671)	0.125 (<i>p</i> = 0.683)
MVD (mm ⁻²)	0.562 (<i>p</i> = 0.010)	0.335 (<i>p</i> = 0.149)	-0.124 (<i>p</i> = 0.791)	0.036 (<i>p</i> = 0.939)	0.078 (<i>p</i> = 0.801)	-0.245 (<i>p</i> = 0.420)
VSI (μm)	0.485 (<i>p</i> = 0.030)	0.401 (<i>p</i> = 0.080)	-0.062 (<i>p</i> = 0.894)	0.148 (<i>p</i> = 0.751)	-0.132 (<i>p</i> = 0.668)	-0.054 (<i>p</i> = 0.861)

OEF: oxygen extraction fraction; CMRO₂: cerebral metabolic rate of oxygen; mitoPO₂: mitochondrial oxygen tension; CBV: cerebral blood volume; μCBV: cerebral blood volume in microvasculature; CBF: cerebral blood flow; μCBF: cerebral blood flow in microvasculature; MVD: microvessel density; VSI: vessel size index.

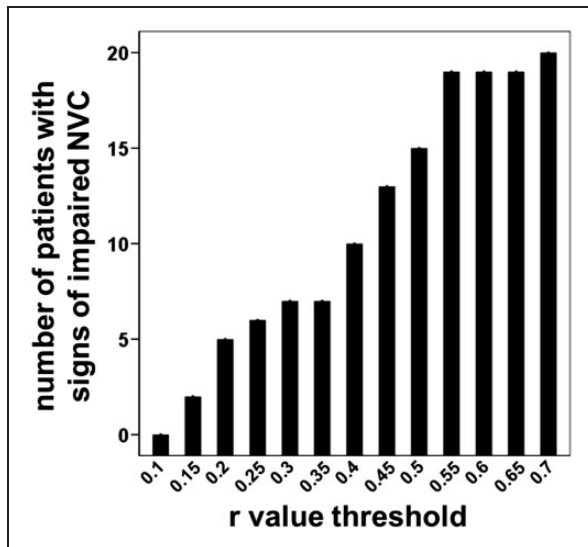


Figure 4. Bar plot demonstrating the relationship between the number of patients with signs of impaired NVC and the *r* value threshold used for BOLD fMRI data processing. A value of 0.3 is commonly used as threshold for correlation. NVC: neurovascular coupling.

regions that, in turn, showed significant brain tissue hypoxia, as well as significantly decreased macro- and microvascular hemodynamics, and microvascular architecture. These seven patients predominantly

suffered from high-grade glioma (six patients), and one patient had a Cav.

Neurosurgeons rely on reliable presurgical mapping of eloquent cortical regions in order to achieve maximum safe resection of brain lesions, i.e. maximize the extent of resection while preserving neurological status of the patient. BOLD fMRI, which is considered as a main method for this purpose, however, is not reliable when the eloquent cortex is in close vicinity to the lesion, i.e. in the most crucial situation. Impairment of NVC, also known as neurovascular uncoupling or decoupling, is widely accepted as reason for impaired BOLD response when mapping these crucial cortical areas and therefore may confound interpretation of BOLD fMRI data.^{8,44,45}

Holodny et al.^{8,46} were one of the first who showed that in brain tumor patients, the activation volumes on ipsilateral side of the tumor were significantly smaller compared to the contralateral, unaffected side. They assumed that a loss of autoregulation in the tumor vasculature and compressive effects to venous structures were the cause for this difference. In order to develop an MRI-based method for detection of neurovascular uncoupling, Pillai and Zaca⁴⁷ used BOLD cerebrovascular reactivity (CVR) mapping during hypercapnia induction via breath-holding in conjunction with task-based fMRI and found an overall concordance of 95% between areas of abnormally decreased

regional CVR with areas of absent BOLD task-based activation in expected eloquent cortical regions infiltrated by or adjacent to the tumors. Hence, they concluded that breath-holding CVR mapping may be an important surrogate marker of NVU potential. However, using this method does not allow for spatial assessment of the functional level of cortical tissue with impaired CVR, i.e. impaired NVC.

Alternatively, in our study, we performed MEG experiments for detection of impaired NVC. Task-evoked fields in cortical areas with attenuated BOLD response have been interpreted as lesion-induced impairment of NVC. This MEG-based approach has been previously used in few studies for this purpose. Rossini et al.¹¹ compared the neuronal activation in 10 patients with cerebrovascular diseases during somatosensory stimulation measured with both MEG and BOLD fMRI and observed neuronal activity in the sensory cortex areas with MEG that was not observed on fMRI in five patients. Furthermore, they demonstrated that this uncoupling of neuronal activity from fMRI activation was strongly associated to the altered vasomotor reactivity as measured by transcranial Doppler during CO₂ inhalation. Further studies that combined BOLD fMRI and MEG during language tasks in patients with focal brain lesions also found MEG activities but missing BOLD response in the fMRI data in 53%¹² and 17%¹⁰ of the patients, respectively. These latter studies, similar to our study, did not use MR-based CVR mapping. Nevertheless, a combination of BOLD fMRI, MEG, and CVR mapping would be of high scientific interest in order to better understand the mechanism of lesion-induced attenuation of the BOLD effect and impairment of the NVC.

In the present study, we were able to uncover physiological reasons for attenuated BOLD response and impaired NVC using an advanced multiparametric MRI method. Our VAM approach revealed alterations in microvascular architecture, i.e. significant decreased MVD and size, in the cortical areas showing attenuated BOLD response. This was associated with significantly decreased hemodynamics in both macro- and microvasculature. Additionally, these cortical regions were affected by altered oxygen metabolism: a significantly increased CMRO₂ and OEF, which was associated with strongly decreased tissue oxygen tension, i.e. severe local hypoxia.

The widely accepted view is that tumor infiltration of the brain parenchyma occurs by cooption of pre-existing vessels.^{48,49} With tumor growth, cancer cells migrate along existing blood vessels and invade the perivascular space.^{49,50} Healthy brain vessels, however, are surrounded by astrocytes, and glioma cell invasion lead to the displacement of the astrocytic end-feet from the vasculature.⁵¹ In addition, glioma cells took over

the areas surrounding blood vessels, particularly favoring small capillaries. This leads to compression and destabilization of the vessels and in further consequence to vessel regression and reduced perfusion.⁵² This is in accordance with our current study findings of reduced CBF and volume as well as decreased MVD and diameter. Additional studies such the work of Watkins et al.⁵¹ suggested that this prevents vasoactive molecules released by astrocytes from reaching the endothelial cells, and glioma cells can increase their invasion area in the perivascular space by inducing vasoconstriction.⁵¹ Ultimately, both effects may lead to an impairment of the NVC (and an attenuated BOLD response). Furthermore, reduced perfusion combined with increasing energy demands of progressing tumors (increased CMRO₂ in our study) results in higher extraction of oxygen (increased OEF in our study) and a paucity of oxygen, i.e. hypoxia (decreased mitoPO₂ in our study).⁴⁹ A study by Sumiyoshi et al.¹⁵ investigated the effects of oxygen availability on NVC using simultaneous electroencephalography (EEG) and BOLD fMRI in anesthetized rats and found that even mild hypoxic conditions induced significant reductions in fMRI responses to electrical stimulation in the forepaw, but EEG responses remained unchanged. It is also well acknowledged that hypoxia plays an important role in the pathophysiology of the neurovascular unit⁵³ in cerebrovascular diseases such as Cav, where thrombosis with associated hypoxia and reactive gliosis of adjacent cerebral parenchyma are frequent signs.⁵⁴

The main limitation of this study is the relatively small sample size of the patient cohort with different tumor pathologies. We presented results of 20 patients with gliomas (low or high-grade), cerebrovascular diseases (AVM or Cav), or a meningioma, respectively. Furthermore, we did not include CVR mapping during breath-holding or CO₂ inhalation, which might be of high scientific and possibly clinical relevance. An additional important limitation is related with the fact that BOLD fMRI was performed at 1.5 tesla. Previous studies investigated the influence of field strength on sensitivity and specificity in BOLD fMRI and demonstrated the advantages of high-field (3 tesla) and ultra-high-field (7 tesla) MR systems.^{55,56} Further studies demonstrated the usefulness and reliability of 7 tesla BOLD fMRI for presurgical planning.^{57,58} Therefore, future studies are highly warranted to replicate our findings on a larger scale including CVR mapping and high-field or ultra-high-field BOLD fMRI. The model for calculation of OEF has also several limitations. It assumes that the system is in the static dephasing regime⁵⁹ which is associated with the fact that OEF is predominantly weighted to the medium-sized and larger vessels of the venous vascular network. Furthermore, the multiparametric qBOLD approach¹⁸

provides an average blood oxygenation within the entire vasculature, which is different from the venous blood oxygenation (deoxygenated CBV) derived from the original qBOLD approach,⁶⁰ and ignores the intravascular component. Additionally, accumulation of hemosiderin and/or proteins in perilesional tissue could bias the OEF estimation. Therefore, it is important to point out that the multiparametric qBOLD approach provides only an estimation of the oxygen metabolism with model-inherent limitations.

Another confounding factor of this study is related to the use of the combined GE-SE perfusion sequence^{19,21} that does not fully meet the requirements for clinical routine diagnosis due to insufficient spatial coverage as only eight slices are measured. The coverage of the whole brain, however, is mandatory for routine MR perfusion. The efforts to upgrade the combined GE-SE perfusion sequence with the promising Simultaneous MultiSlice technique for full coverage may help to overcome these restrictions.⁶¹ In previous studies, we used two separate MR perfusion sequences, i.e. one for GE-EPI DSC perfusion and one for SE-EPI DSC perfusion measurements instead of the hybrid GESE EPI perfusion sequence used in this study. The approach with two separate MR perfusion sequences, however, provides full compatibility with the efforts of clinical routine MRI.^{23,24,26}

Conclusion

Conclusively, our multimodal preoperative mapping approach combining fMRI and MEG provided highly consistent evidence for the presence of lesion-induced impairment of NVC in functional important cortex areas adjacent to brain lesions. This is of high clinical relevance for preoperative planning and postoperative outcome. However, due to the limited availability of MEG devices and the time-consuming implementation of MEG experiments, it is not used routinely in clinical practice. Our physiological MRI approach, which required only a few minutes of extra scanning time, may allow the detection of cortical areas at risk for lesion-induced impairment of NVC. However, CVR mapping should be included in future studies.

Funding

The author(s) disclosed receipt of the following financial support for the research, authorship, and/or publication of this article: This work was supported by the German Research Foundation (Deutsche Forschungsgemeinschaft; Grant Numbers STA 1331/3-1 and DO 721/9-1) and by the Erlanger Leistungsbezogene Anschubfinanzierung und

Nachwuchsförderung program (Grant Number 14-05-21-1-Stadlbauer).

Acknowledgements

We thank Martin Kaltenhäuser and Peter Grummich, from the Department of Neurosurgery of the University Clinic Erlangen, for technical assistance.


Declaration of conflicting interests


The author(s) declared no potential conflicts of interest with respect to the research, authorship, and/or publication of this article.

Authors' contributions

AS, TMK, AD, MB, MZi, MZa, NB, SB, and IE conceived the study. AS, SB, IE, MZi, MZa, NB, and TMK were involved in the analysis of the data. AS, TMK, AD, MZi, NB, IE, and SB were involved in the interpretation of the data. AS, MB, MZi, NB, and AD contributed to the acquisition of the data. All authors reviewed the manuscript critically for intellectual content, and read and approved the final manuscript.

ORCID iDs

Andreas Stadlbauer  <https://orcid.org/0000-0001-8348-2620>

Thomas M Kinfe  <https://orcid.org/0000-0002-4888-543X>

References

- Ogawa S, Menon RS, Tank DW, et al. Functional brain mapping by blood oxygenation level-dependent contrast magnetic resonance imaging. A comparison of signal characteristics with a biophysical model. *Biophys J* 1993; 64: 803–812.
- Ogawa S, Lee TM, Kay AR, et al. Brain magnetic resonance imaging with contrast dependent on blood oxygenation. *Proc Natl Acad Sci U S A* 1990; 87: 9868–9872.
- Hu X and Yacoub E. The story of the initial dip in fMRI. *Neuroimage* 2012; 62: 1103–1108.
- Gabriel M, Brennan NP, Peck KK, et al. Blood oxygen level dependent functional magnetic resonance imaging for presurgical planning. *Neuroimaging Clin N Am* 2014; 24: 557–571.
- Filippi M and Agosta F. Diffusion tensor imaging and functional MRI. *Handb Clin Neurol* 2016; 136: 1065–1087.
- Chaudhry AA, Naim S, Gul M, et al. Utility of preoperative blood-oxygen-level-dependent functional MR imaging in patients with a central nervous system neoplasm. *Radiol Clin North Am* 2019; 57: 1189–1198.
- Pak RW, Hadjiabadi DH, Senarathna J, et al. Implications of neurovascular uncoupling in functional magnetic resonance imaging (fMRI) of brain tumors. *J Cereb Blood Flow Metab* 2017; 37: 3475–3487.
- Holodny AI, Schulder M, Liu WC, et al. The effect of brain tumors on BOLD functional MR imaging activation in the adjacent motor cortex: implications for

- image-guided neurosurgery. *Am J Neuroradiol* 2000; 21: 1415–1422.
9. Hari R, Parkkonen L and Nangini C. The brain in time: insights from neuromagnetic recordings. *Ann N Y Acad Sci* 2010; 1191: 89–109.
 10. Zimmermann M, Rössler K, Kaltenhäuser M, et al. Refined functional magnetic resonance imaging and magnetoencephalography mapping reveals reorganization in language-relevant areas of lesioned brains. *World Neurosurg* 2020; 136: e41–e59.
 11. Rossini PM, Altamura C, Ferretti A, et al. Does cerebrovascular disease affect the coupling between neuronal activity and local haemodynamics? *Brain* 2004; 127: 99–110.
 12. Grummich P, Nimsky C, Pauli E, et al. Combining fMRI and MEG increases the reliability of presurgical language localization: a clinical study on the difference between and congruence of both modalities. *Neuroimage* 2006; 32: 1793–1803.
 13. Para AE, Sam K, Poublanc J, et al. Invalidation of fMRI experiments secondary to neurovascular uncoupling in patients with cerebrovascular disease. *J Magn Reson Imaging* 2017; 46: 1148–1455.
 14. Orukari IE, Siegel JS, Warrington NM, et al. Altered hemodynamics contribute to local but not remote functional connectivity disruption due to glioma growth. *J Cereb Blood Flow Metab* 2020; 40: 100–115.
 15. Sumiyoshi A, Suzuki H, Shimokawa H, et al. Neurovascular uncoupling under mild hypoxic hypoxia: an EEG-fMRI study in rats. *J Cereb Blood Flow Metab* 2012; 32: 1853–1858.
 16. Stadlbauer A, Zimmermann M, Kitzwögerer M, et al. MR imaging-derived oxygen metabolism and neovascularization characterization for grading and IDH gene mutation detection of gliomas. *Radiology* 2017; 283: 799–809.
 17. Stadlbauer A, Zimmermann M, Heinz G, et al. Magnetic resonance imaging biomarkers for clinical routine assessment of microvascular architecture in glioma. *J Cereb Blood Flow Metab* 2017; 37: 632–643.
 18. Christen T, Schmiedeskamp H, Straka M, et al. Measuring brain oxygenation in humans using a multiparametric quantitative blood oxygenation level dependent MRI approach. *Magn Reson Med* 2012; 68: 905–911.
 19. Xu C, Kiselev VG, Möller HE, et al. Dynamic hysteresis between gradient echo and spin echo attenuations in dynamic susceptibility contrast imaging. *Magn Reson Med* 2013; 69: 981–991.
 20. Kiselev VG, Strecker R, Ziyeh S, et al. Vessel size imaging in humans. *Magn Reson Med* 2005; 53: 553–563.
 21. Emblem KE, Mouridsen K, Bjornerud A, et al. Vessel architectural imaging identifies cancer patient responders to anti-angiogenic therapy. *Nat Med* 2013; 19: 1178–1183.
 22. Stadlbauer A, Zimmermann M, Oberndorfer S, et al. Vascular hysteresis loops and vascular architecture mapping in patients with glioblastoma treated with antiangiogenic therapy. *Sci Rep* 2017; 7: 8508.
 23. Stadlbauer A, Zimmermann M, Doerfler A, et al. Intratumoral heterogeneity of oxygen metabolism and neovascularization uncovers 2 survival-relevant subgroups of IDH1 wild-type glioblastoma. *Neuro Oncol* 2018; 20: 1536–1546.
 24. Stadlbauer A, Roessler K, Zimmermann M, et al. Predicting glioblastoma response to bevacizumab through MRI biomarkers of the tumor microenvironment. *Mol Imaging Biol* 2019; 21: 747–757.
 25. Stadlbauer A, Mouridsen K, Doerfler A, et al. Recurrence of glioblastoma is associated with elevated microvascular transit time heterogeneity and increased hypoxia. *J Cereb Blood Flow Metab* 2018; 38: 422–432.
 26. Stadlbauer A, Oberndorfer S, Zimmermann M, et al. Physiologic MR imaging of the tumor microenvironment revealed switching of metabolic phenotype upon recurrence of glioblastoma in humans. *J Cereb Blood Flow Metab* 2020; 40: 528–538.
 27. Prasloski T, Mädler B, Xiang QS, et al. Applications of stimulated echo correction to multicomponent T2 analysis. *Magn Reson Med* 2012; 67: 1803–1814.
 28. Bjornerud A and Emblem KE. A fully automated method for quantitative cerebral hemodynamic analysis using DSC-MRI. *J Cereb Blood Flow Metab* 2010; 30: 1066–1078.
 29. Boxerman JL, Prah DE, Paulson ES, et al. The role of preload and leakage correction in gadolinium-based cerebral blood volume estimation determined by comparison with MION as a criterion standard. *Am J Neuroradiol* 2012; 33: 1081–1087.
 30. Vafaei MS, Vang K, Bergersen LH, et al. Oxygen consumption and blood flow coupling in human motor cortex during intense finger tapping: implication for a role of lactate. *J Cereb Blood Flow Metab* 2012; 32: 1859–1868.
 31. Kennan RP, Zhong J and Gore JC. Intravascular susceptibility contrast mechanisms in tissues. *Magn Reson Med* 1994; 31: 9–21.
 32. Vafaei MS and Gjedde A. Model of blood-brain transfer of oxygen explains nonlinear flow-metabolism coupling during stimulation of visual cortex. *J Cereb blood flow Metab* 2000; 20: 747–754.
 33. Ducreux D, Buvat I, Meder JF, et al. Perfusion-weighted MR imaging studies in brain hypervascular diseases: comparison of arterial input function extractions for perfusion measurement. *AJNR Am J Neuroradiol* 2006; 27: 1059–1069.
 34. Jensen JH, Lu H and Inglese M. Microvessel density estimation in the human brain by means of dynamic contrast-enhanced echo-planar imaging. *Magn Reson Med* 2006; 56: 1145–1150.
 35. Zimmermann M, Rössler K, Kaltenhäuser M, et al. Comparative fMRI and MEG localization of cortical sensorimotor function: bimodal mapping supports motor area reorganization in glioma patients. *PLoS One* 2019; 14: e0213371.
 36. Thesen S, Heid O, Mueller E, et al. Prospective acquisition correction for head motion with image-based

- tracking for real-time fMRI. *Magn Reson Med* 2000; 44: 457–465.
37. Bandettini PA, Jesmanowicz A, Wong EC, et al. Processing strategies for time-course data sets in functional MRI of the human brain. *Magn Reson Med* 1993; 30: 161–173.
 38. Castillo EM, Simos PG, Wheless JW, et al. Integrating sensory and motor mapping in a comprehensive MEG protocol: clinical validity and replicability. *Neuroimage* 2004; 21: 973–983.
 39. Shattuck DW and Leahy RM. Brainsuite: an automated cortical surface identification tool. *Med Image Anal* 2002; 6: 129–142.
 40. Dale AM, Liu AK, Fischl BR, et al. Dynamic statistical parametric mapping: combining fMRI and MEG for high-resolution imaging of cortical activity. *Neuron* 2000; 26: 55–67.
 41. Tadel F, Baillet S, Mosher JC, et al. Brainstorm: a user-friendly application for MEG/EEG analysis. *Comput Intell Neurosci* 2011; 2011: 879716.
 42. Dale AM and Sereno MI. Improved localization of cortical activity by combining EEG and MEG with MRI cortical surface reconstruction: a linear approach. *J Cogn Neurosci* 1993; 5: 162–176.
 43. Greenblatt RE, Ossadtchi A and Pflieger ME. Local linear estimators for the bioelectromagnetic inverse problem. *IEEE Trans Signal Process* 2005; 53: 3403–3412.
 44. Zaca D, Jovicich J, Nadar SR, et al. Cerebrovascular reactivity mapping in patients with low grade gliomas undergoing presurgical sensorimotor mapping with BOLD fMRI. *J Magn Reson Imaging* 2014; 40: 383–390.
 45. Agarwal S, Sair HI, Yahyavi-Firouz-Abadi N, et al. Neurovascular uncoupling in resting state fMRI demonstrated in patients with primary brain gliomas. *J Magn Reson Imaging* 2016; 43: 620626.
 46. Holodny AI, Schulder M, Liu WC, et al. Decreased BOLD functional MR activation of the motor and sensory cortices adjacent to a glioblastoma multiforme: implications for image-guided neurosurgery. *Am J Neuroradiol* 1999; 20: 609–612.
 47. Pillai JJ and Zaca D. Comparison of BOLD cerebrovascular reactivity mapping and DSC MR perfusion imaging for prediction of neurovascular uncoupling potential in brain tumors. *Technol Cancer Res Treat* 2012; 11: 361–374.
 48. Leenders WPJ, Küsters B and De Waal RMW. Vessel cooption: how tumors obtain blood supply in the absence of sprouting angiogenesis. *Endothel J Endothel Cell Res* 2002; 9: 83–87.
 49. Holash J, Maisonpierre PC, Compton D, et al. Vessel cooption, regression, and growth in tumors mediated by angiopoietins and VEGF. *Science (80-)* 1999; 284: 1994–1998.
 50. Hardee ME and Zagzag D. Mechanisms of glioma-associated neovascularization. *Am J Pathol* 2012; 181: 1126–1141.
 51. Watkins S, Robel S, Kimbrough IF, et al. Disruption of astrocyte-vascular coupling and the blood-brain barrier by invading glioma cells. *Nat Commun* 2014; 5: 1–15.
 52. Padera TP, Stoll BR, Tooredman JB, et al. Cancer cells compress intratumour vessels. *Nature* 2004; 427: 695.
 53. Stanimirovic DB and Friedman A. Pathophysiology of the neurovascular unit: disease cause or consequence. *J Cereb Blood Flow Metab* 2012; 32: 1207–1221.
 54. Cortés Vela JJ, Concepción Aramendía L, Ballenilla Marco F, et al. Cerebral cavernous malformations: spectrum of neuroradiological findings. *Radiol (English Ed)* 2012; 54: 401–409.
 55. Boubela RN, Kalcher K, Nasel C, et al. Scanning fast and slow: current limitations of 3 Tesla functional MRI and future potential. *Front Phys* 2014; 2: 00001.
 56. Beisteiner R, Robinson S, Wurnig M, et al. Clinical fMRI: evidence for a 7T benefit over 3T. *Neuroimage* 2011; 57: 1015–1021.
 57. Cardoso PL, Fischmeister FPS, Dymerska B, et al. Improving the clinical potential of ultra-high field fMRI using a model-free analysis method based on response consistency. *Magn Reson Mater Physics, Biol Med* 2016; 29: 435–449.
 58. Lima Cardoso P, Fischmeister FPS, Dymerska B, et al. Robust presurgical functional MRI at 7 T using response consistency. *Hum Brain Mapp* 2017; 38: 3163–3174.
 59. Yablonskiy DA and Haacke EM. Theory of NMR signal behavior in magnetically inhomogeneous tissues: the static dephasing regime. *Magn Reson Med* 1994; 32: 749–763.
 60. He X and Yablonskiy DA. Quantitative BOLD: mapping of human cerebral deoxygenated blood volume and oxygen extraction fraction: default state. *Magn Reson Med* 2007; 57: 115–126.
 61. Eichner C, Jafari-Khouzani K, Cauley S, et al. Slice accelerated gradient-echo spin-echo dynamic susceptibility contrast imaging with blipped CAIPI for increased slice coverage. *Magn Reson Med* 2013; 72: 770–778.